Dalton Transactions

ROYAL SOCIETY OF CHEMISTRY

PAPER

View Article Online
View Journal | View Issue

Cite this: *Dalton Trans.*, 2026, **55**, 2509

Structure-DFT-bioactivity correlation in mixed-ligand Fe(III), Mn(II), and V(IV)O complexes with bidentate NO donor 1*H*-benzimidazole-2-carboxylic acid and norfloxacin ligands

Hany M. Abd El-Lateef, *[a] Mai M. Khalaf*[a] and Aly Abdou *[b]

Three new mixed-ligand transition-metal complexes of iron(III), manganese(II), and oxidovanadium(IV) were synthesized using 1*H*-benzimidazole-2-carboxylic acid and 1-ethyl-6-fluoro-4-oxo-7-(piperazin-1-yl)-1,4-dihydroquinoline-3-carboxylic acid (norfloxacin) as coordinating ligands. The complexes were characterized by elemental analysis, infrared and electronic spectroscopy, mass spectrometry, molar conductance, magnetic measurements, and thermal analysis. Spectroscopic results indicate bidentate coordination of both ligands through nitrogen and oxygen donor atoms, leading to octahedral geometries for the iron(III) and manganese(II) complexes and a square-pyramidal geometry for the oxidovanadium(IV) complex. Molar conductance data support the non-electrolytic nature of the complexes, while magnetic measurements are consistent with the proposed coordination environments. Thermal studies confirmed the presence or absence of coordinated water molecules, in agreement with the suggested formulations. Density functional theory calculations revealed changes in frontier molecular orbital energies and global reactivity descriptors upon coordination, indicating modified electronic properties relative to the free ligands. *In vitro* antimicrobial studies showed that the metal complexes exhibited higher antibacterial and antifungal activities than the uncoordinated ligands, with inhibition zones comparable to those of a reference antibacterial drug. Anti-inflammatory evaluation demonstrated notable inhibitory effects for the oxidovanadium(IV) and manganese(II) complexes. Molecular docking studies suggested favorable interactions of the iron(III) and oxidovanadium(IV) complexes with DNA gyrase B, providing a possible molecular basis for the observed antibacterial trends. Overall, the results demonstrate that metal coordination significantly influences the structural, electronic, and biological properties of the ligand system.

Received 24th October 2025,
Accepted 3rd January 2026

DOI: 10.1039/d5dt02558c

rsc.li/dalton

1. Introduction

In an era marked by the escalating threat of antimicrobial resistance[1–3] and the rising incidence of inflammatory diseases,[4,5] the search for innovative therapeutic strategies has become increasingly urgent. The diminishing efficacy of conventional antibiotics against resistant microbial strains,[6,7] together with the global burden of chronic inflammatory disorders,[8] has stimulated growing interest in alternative therapeutic approaches. In this context, metal-based compounds have emerged as promising candidates due to their diverse coordination geometries, tunable redox properties, and ability to modulate the biological activity of organic ligands.

Fluoroquinolone antibiotics, such as 1-ethyl-6-fluoro-4-oxo-7-piperazin-1-yl-1,4-dihydroquinoline-3-carboxylic acid (norfloxacin), are well known for their broad-spectrum antibacterial activity through inhibition of bacterial type II topoisomerases, particularly DNA gyrase and topoisomerase IV.[9–11] Despite their clinical importance, the therapeutic performance of fluoroquinolones can be limited by poor physicochemical properties and the rapid emergence of resistant strains. In parallel, 1*H*-benzimidazole-2-carboxylic acid has attracted considerable attention owing to its reported antibacterial, antifungal, and anti-inflammatory activities, which are attributed to its heterocyclic nitrogen donor system and ability to interact with biological targets.[12–14] The incorporation of these two bioactive ligands into a single coordination framework offers an attractive strategy for modulating biological performance through metal–ligand synergy.

Transition metals such as iron, manganese, and vanadium play essential roles in biological systems and have been widely explored in medicinal inorganic chemistry.[15–18] Iron complexes have demonstrated notable antibacterial and anti-

[a]*Department of Chemistry, College of Science, King Faisal University, Al-Ahsa 31982, Saudi Arabia. E-mail: hmahmed@kfu.edu.sa*
[b]*Department of Chemistry, Faculty of Science, Sohag University, Sohag 82524, Egypt. E-mail: aly_abdou@science.sohag.edu.eg*

inflammatory properties, often associated with their redox activity and capacity to interfere with microbial metabolic pathways. Manganese is a biologically indispensable element involved in antioxidant defense, enzymatic catalysis, and immune regulation. Importantly, manganese complexes have been reported to exhibit antibacterial and antifungal activities, as well as anti-inflammatory effects, linked to their ability to modulate reactive oxygen species and mimic metalloenzymes such as superoxide dismutase.[19–23]

Vanadium, particularly in the oxidovanadium(IV) form, has been extensively studied for its biological activity, including antimicrobial, anti-inflammatory, and enzyme-inhibitory properties. Oxidovanadium(IV) complexes are known to interact with biomolecular targets through coordination and redox mechanisms, making them attractive candidates for biological investigations.[24–27] These characteristics make iron(III), manganese(II), and oxidovanadium(IV) suitable metal centers for the development of biologically relevant coordination compounds.

In antibacterial studies, DNA gyrase B represents a well-established molecular target, as it plays a critical role in bacterial DNA replication and cell viability.[28] Compounds capable of interacting with this enzyme can disrupt bacterial proliferation, and fluoroquinolone-derived ligands are particularly relevant in this context. Therefore, DNA gyrase B was selected as a molecular docking target in this study to provide mechanistic insight into the observed antibacterial trends.

To complement the experimental investigations, density functional theory calculations and molecular docking studies were employed. Theoretical calculations were used to analyze electronic structures and global reactivity descriptors, while docking simulations were applied to explore possible ligand–protein interaction modes without implying direct biological validation.

Accordingly, this work focuses on the design, synthesis, and comprehensive characterization of new iron(III), manganese(II), and oxidovanadium(IV) mixed-ligand complexes derived from 1*H*-benzimidazole-2-carboxylic acid and norfloxacin. This study aims to elucidate their structural and electronic features and to evaluate their antibacterial, antifungal, and anti-inflammatory activities, with the goal of establishing structure–activity relationships and understanding how metal coordination influences biological behavior.

2. Methodology

2.1. Synthesis

2.1.1. Materials. All chemicals and reagents utilized in the synthesis of FeBCNR, MnBCNR, and VOBCNR are provided in the SI.

2.1.2. Preparation of the metal complexes. The synthesis of the mixed-ligand complexes of iron(III), manganese(II), and oxidovanadium(IV), FeBCNR, MnBCNR, and VOBCNR, respectively, was carried out according to the following protocol. An aqueous solution (15.0 mL) of the appropriate metal salt, iron(III) chloride hexahydrate ($FeCl_3{\cdot}6H_2O$, 2.0 mmol), manganese(II) chloride dihydrate ($MnCl_2{\cdot}2H_2O$, 2.0 mmol), or vanadyl acetylacetonate [$VO(acac)_2$, 2.0 mmol] was freshly prepared under gentle stirring. This solution was added dropwise to a hot ethanolic solution (15.0 mL) containing equimolar quantities of norfloxacin (NR, 2.0 mmol) and 1*H*-benzimidazole-2-carboxylic acid (BC, 2.0 mmol), which had been previously mixed and slightly warmed to increase ligand solubility. The resulting mixture was refluxed under continuous magnetic stirring at 80 °C for 5 hours, during which the reaction mixture gradually developed a distinct color characteristic of each complex, indicating successful metal–ligand coordination. Upon completion, the mixture was cooled to room temperature, and the resulting product was filtered off, washed several times with ethanol to remove any unreacted ligands or residual salts, and finally dried in a desiccator over anhydrous calcium chloride. The obtained products were stable, non-hygroscopic, and finely crystalline in nature. The overall synthetic pathway for the preparation of FeBCNR, MnBCNR, and VOBCNR is schematically illustrated in Scheme 1.

[Fe(BC-H)(NR-H)(Cl)(H_2O)]. Brownish-red solid; yield: 80%. Melting point: >300 °C (decomposes). Molar conductance (ethanol): 9.85 Ω^{-1} cm^2 mol^{-1}. Magnetic moment: 1.86 B.M. Elemental analysis (%): found (calculated): C 49.22 (49.96), H 4.86 (4.11), N 12.35 (11.89), Fe 10.11 (9.49). Infrared spectrum (cm^{-1}): ν(C═N) BC, 1571 (shifted from 1624), ν(C═O) NR, 1580 (shifted from 1631), $\nu_{as}(COO^-)$ 1620, $\nu_s(COO^-)$ 1410, $\Delta\nu$ = 210 cm^{-1}, ν(Fe–O) 567, ν(Fe–N) 507.

[Mn(BC-H)(NR-H)(H_2O)$_2$]. Pale pink solid; yield: 81%. Melting point: >300 °C (decomposes). Molar conductance (ethanol): 9.03 Ω^{-1} cm^2 mol^{-1}. Magnetic moment: 1.81 B.M. Elemental analysis (%): found (calculated): C 50.01 (50.53), H 5.15 (4.59), N 11.66 (12.28), Mn 10.28 (9.63). Infrared spectrum (cm^{-1}): ν(C═N) BC 1568, ν(C═O) NR 1595, $\nu_{as}(COO^-)$ 1623, $\nu_s(COO^-)$ 1409, $\Delta\nu$ = 214 cm^{-1}, ν(Mn–O) 560, ν(Mn–N) 511.

[VO(BC-H)(NR-H)]. Pale green solid; yield: 80%. Melting point: >300 °C (decomposes). Molar conductance (ethanol): 9.42 Ω^{-1} cm^2 mol^{-1}. Magnetic moment: 1.77 B.M. Elemental analysis (%): found (calculated): C 53.29 (52.76), H 4.88 (4.06), N 13.34 (12.82), V 9.86 (9.32). Infrared spectrum (cm^{-1}): ν(C═N) BC 1570, ν(C═O) NR 1588, ν(V═O) 960, $\nu_{as}(COO^-)$ 1621, $\nu_s(COO^-)$ 1405, $\Delta\nu(\nu(-COO)_{as}-\nu(-COO)_s)$ = 216 cm^{-1}, ν(V–O) 960, ν(V–N) 509.

2.1.3. Structural characterization. The synthesized FeBCNR, MnBCNR, and VOBCNR were comprehensively characterized using a combination of physicochemical and spectroscopic techniques, as illustrated in the SI, and elemental analysis and atomic absorption spectroscopy were performed to confirm the composition. Infrared spectroscopy was employed to identify coordination modes, while ultraviolet-visible spectroscopy provided insight into electronic transitions. Mass spectrometry was used to verify molecular weights and fragmentation patterns. Thermogravimetric and differential thermal analyses were applied to evaluate thermal stability and the presence of coordinated species. Molar conductance measurements and magnetic susceptibility studies were carried out to assess the electrolytic nature and electronic configurations of the complexes.

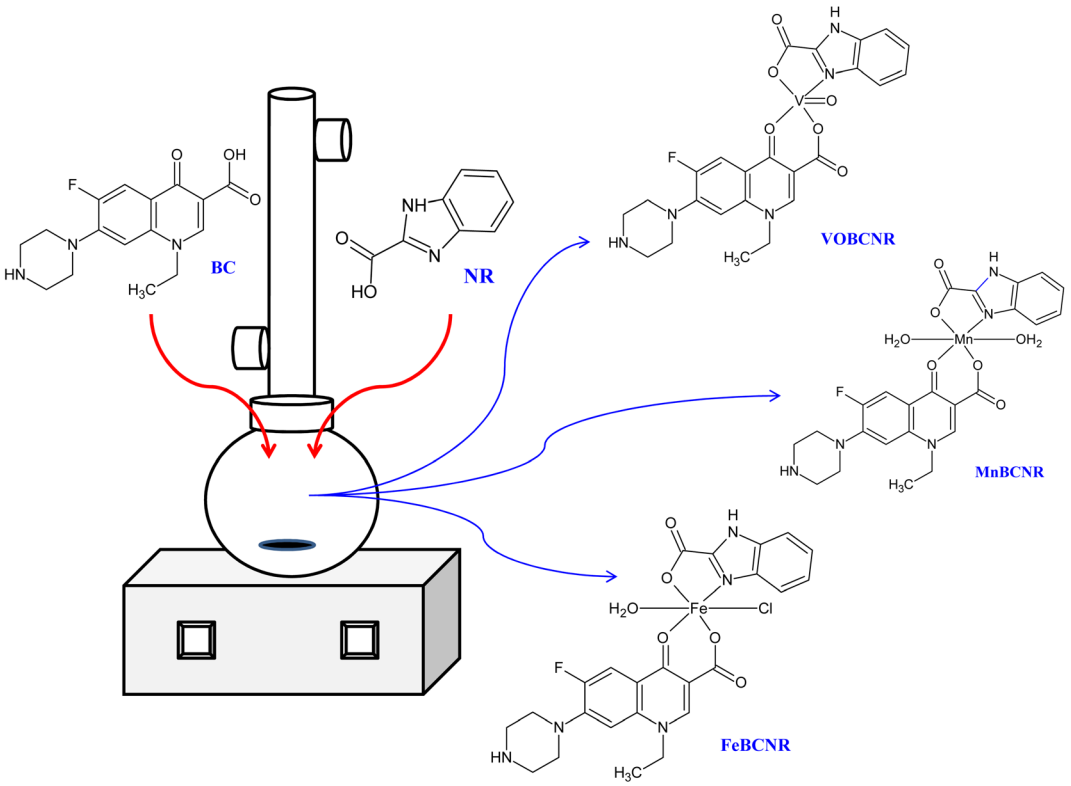

Scheme 1 The overall synthetic pathway for the preparation of FeBCNR, MnBCNR, and VOBCNR.

2.2. DFT calculations

All quantum chemical calculations for the free ligands (BC and NR) and their complexes (FeBCNR, MnBCNR, and VOBCNR) were performed using the ORCA 6.1.0.[29] The geometrical optimization was carried out within the framework of Density Functional Theory (DFT) employing the B3LYP hybrid functional. The def2-TZVP basis set was applied to all non-metal atoms (C, H, N, and O), while the def2-SVP basis set was employed for the transition-metal centers.[30–32] The initial molecular geometries and corresponding input files were generated using the Avogadro molecular modeling package.[33] Upon completion of geometry optimization, the frontier molecular orbitals (HOMO and LUMO) were visualized and analyzed using the Multiwfn program.[34] The global reactivity descriptors, ionization potential (IP), electron affinity (EA), energy gap (ΔE), electronegativity (χ), chemical potential (μ), chemical hardness (η), softness (σ), electrophilicity index (ω), and nucleophilicity (Nu), were calculated,[35–37] see eqn (S1)–(S9), SI. These parameters provided crucial insights into the reactivity and electronic behavior of the ligands and their complexes.

2.3. Biological activity

The detailed experimental methodologies employed for the evaluation of *in vitro* antimicrobial (both antibacterial and antifungal) and anti-inflammatory activities of the NR and BC ligands, along with their FeBCNR, MnBCNR, and VOBCNR complexes, are comprehensively described in the SI.

2.4. Molecular docking

The molecular docking protocol applied to the investigated ligands (BC and NR) and their complexes (FeBCNR, MnBCNR, and VOBCNR) is comprehensively described in the SI. Molecular docking studies were conducted against DNA gyrase (PDB ID: 5MMN). DNA gyrase is a clinically relevant bacterial enzyme essential for DNA replication, making it a standard target for antibacterial drug design. PDB ID 5MMN, corresponding to the 24 kDa ATPase domain of *E. coli* DNA gyrase B, was chosen due to its well-characterized crystal structure and known inhibitor complex, providing a reliable model for evaluating potential ligand interactions.

3. Results and discussion

3.1. Structural characterization

The physical appearance and basic thermal properties of the isolated complexes provide initial insights into their composition and purity. These complexes are characterized as powder solids with high melting points exceeding 300 °C and good yields: FeBCNR at 80%, MnBCNR at 81%, and VOBCNR at 80% (see Table S1).

Elemental analyses (see Table S2) were used in conjunction with atomic absorption spectroscopy, mass spectrometry, and

thermogravimetric analysis to establish the compositions of the complexes. Given the presence of coordinated water molecules and halide ligands, slight deviations from the calculated CHN values may occur; therefore, structural assignments were validated using multiple independent physicochemical techniques. The found and calculated values are consistent. This close agreement supports the proposed molecular formulas of the neutral complexes as $C_{24}H_{24}ClFeN_5O_6$ for FeBCNR, $C_{24}H_{26}MnN_5O_7$ for MnBCNR, and $C_{24}H_{22}VN_5O_6$ for VOBCNR.

Infrared spectroscopy was employed to investigate the donor atoms and coordination modes of the synthesized complexes, Table 1. Upon coordination, significant spectral shifts were observed. The azomethine –C═N stretching band of free 1*H*-benzimidazole-2-carboxylic acid (BC) at 1624 cm^{-1} shifted to 1570–1571 cm^{-1} in the complexes, indicating coordination through the azomethine nitrogen. Similarly, the carbonyl stretching of norfloxacin (NR) at 1631 cm^{-1} shifted to 1580–1595 cm^{-1}, consistent with binding *via* the carbonyl oxygen.

The carboxylate group coordination mode was assessed from the difference between the asymmetric and symmetric stretching vibrations, $\nu_{as}(COO^-)$ and $\nu_s(COO^-)$. In the complexes, $\nu_{as}(COO^-)$ appears in the range of 1620–1623 cm^{-1}, while $\nu_s(COO^-)$ is observed at 1405–1410 cm^{-1}, yielding $\Delta\nu$ values of 210–216 cm^{-1}. These values are consistent with a monodentate carboxylate coordination mode.[38,39] In the oxidovanadium(IV) complex, a distinct and intense band at approximately 960 cm^{-1} is assigned to the terminal ν(V═O) stretching vibration, a diagnostic feature of oxidovanadium(IV) complexes,[40–42] while the V–O(ligand) and V–N vibrations were observed in the 509–562 cm^{-1} region. This band confirms the presence of a V═O unit and supports a square-pyramidal geometry around the vanadium center. New metal–ligand bands were observed at 507–511 cm^{-1} for M–N and 560–567 cm^{-1} for M–O (Fe–O and Mn–O). Overall, the IR data confirm that both ligands act as bidentate NO donors, coordinating through one nitrogen atom from the C═N group and one oxygen atom from the carboxylate or carbonyl groups.

Magnetic susceptibility measurements yield small but informative values. The effective magnetic moments are μ_{eff} (FeBCNR) = 1.86 B.M., μ_{eff} (MnBCNR) = 1.81 B.M., and μ_{eff} (VOBCNR) = 1.77 B.M. (see Table S3). The value for FeBCNR is indicative of a low-spin Fe(III) (t_{2g}^5) with one unpaired electron, supporting the octahedral geometry suggested by the UV-Vis data. The low value for MnBCNR is atypical for Mn(II); yet, the measured μ_{eff} of approximately 1.8 B.M. suggests that MnBCNR behaves as a low-spin d^5 species (one unpaired electron), indicating a strong ligand field in an octahedral arrangement. The VOBCNR value near 1.77 B.M. corresponds to a V(IV) O d^1 species (one unpaired electron) in a square-pyramidal environment, further corroborating the geometries inferred from the spectroscopic data.

Thermogravimetric (TG) and differential thermogravimetric (DTG) analyses of the FeBCNR, MnBCNR, and VOBCNR complexes were conducted to assess their thermal stability and to identify the presence of coordinated or hydrated water molecules (see Fig. 1 and Table 2). The FeBCNR complex exhibited four distinct thermal decomposition stages. The first step occurred between 165 and 225 °C, with a DTG peak at 172 °C, showing a 3.054% experimental mass loss (calculated 3.841%), corresponding to the elimination of one coordinated water molecule. The subsequent decomposition stages occurred at 225–315 °C (DTG 265 °C), 315–480 °C (DTG 375 °C), and 480–680 °C (DTG 570 °C), with mass losses of 19.375% (19.003%), 20.553% (21.105%), and 44.724% (45.332%), respectively. These losses are attributed to the sequential degradation of organic moieties as $C_6H_{14}N_2$, C_8H_6F, and $C_{10}H_2ClN_3O_4$, respectively, leaving a final residue of 12.182% (12.724%), corresponding to $0.5Fe_2O_3$.

Similarly, the MnBCNR complex decomposed through four distinct stages. The first mass loss occurred between 165 and 220 °C (DTG 175 °C), showing a 6.301% loss (calculated 6.932%), consistent with the removal of two coordinated water molecules. The subsequent decomposition stages appeared at 220–335 °C (DTG 270 °C), 335–480 °C (DTG 365 °C), and 480–675 °C (DTG 540 °C), with corresponding mass losses of 19.986% (20.342%), 21.202% (21.884%), and 39.931% (40.634%), attributed to the elimination of $C_6H_{14}N_2$, C_8H_6F, and $C_{10}H_2N_3O_4$ fragments, respectively. The thermal residue amounted to 12.416% (12.416–23.216%), indicating the formation of MnO as the final decomposition product.

In contrast, the VOBCNR complex exhibited only three main decomposition stages, with no initial weight loss at lower temperatures, confirming the absence of coordinated or lattice water molecules. The first major decomposition occurred between 205 and 340 °C (DTG 260 °C), with a

Table 1 IR data of the BC and NR ligands and FeBCNR, MnBCNR, and VOBCNR complexes

	Ligands		Complexes		
	BC	NR	FeBCNR	MnBCNR	VOBCNR
ν(–C═N)$_{BC}$	1624	—	1571	1568	1570
ν(–C═O)$_{NR}$	—	1631	1580	1595	1588
ν(–COO)$_{as}$	1685	1701	1620	1623	1621
ν(–COO)$_s$	—	—	1410	1409	1405
ν(–COO)$_{as}$–ν(–COO)$_s$	—	—	210	214	216
ν(M–O)	—	—	567	560	960
ν(M–N)	—	—	507	511	509

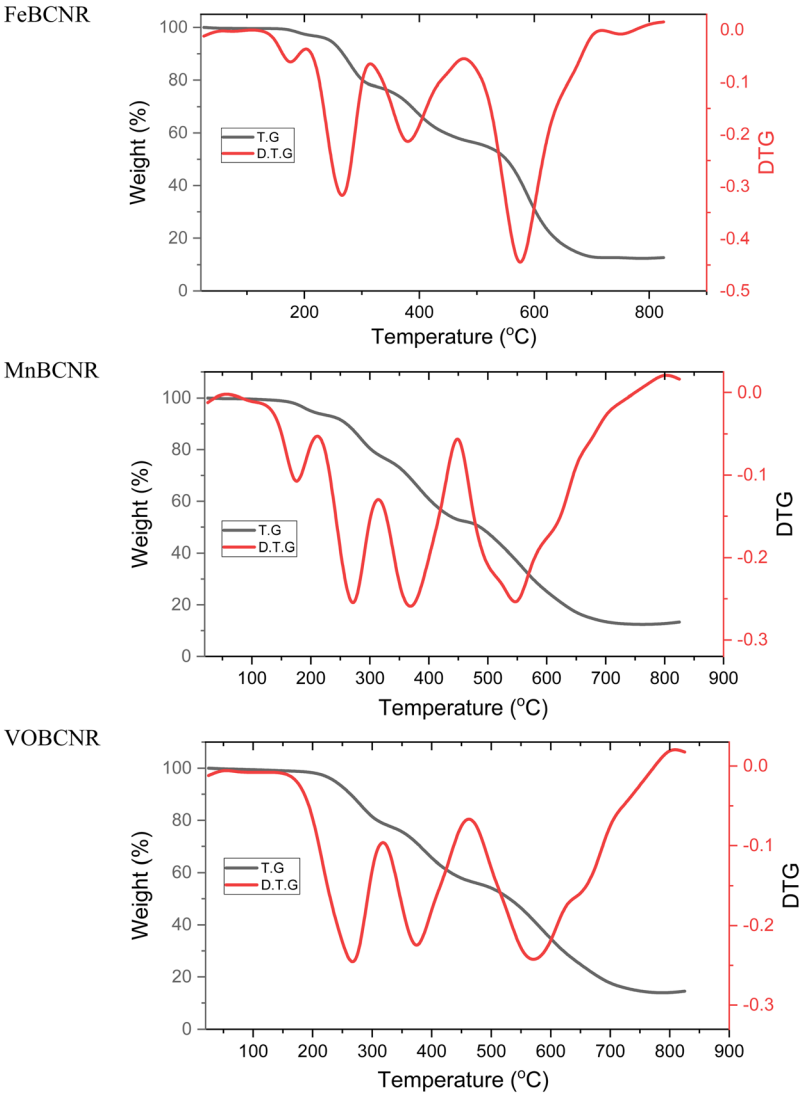

Fig. 1 Thermal degradation of FeBCNR, MnBCNR, and VOBCNR.

Table 2 Thermal degradation data of the FeBCNR, MnBCNR, and VOBCNR complexes

			Mass loss (%)		Residue (%)	
	TG (°C)	DTG (°C)	Found (calculated)	Assignment	Found (calculated)	Assignment
FeBCNR	165–225	172	3.054 (3.841)	H_2O	96.841 (97.441)	$C_{24}H_{22}ClFFeN_5O_5$
	225–315	265	19.375 (19.003)	$C_6H_{14}N_2$	77.467 (77.042)	$C_{18}H_8ClFFeN_3O_5$
	315–480	375	20.553 (21.105)	C_8H_6F	56.914 (57.653)	$C_{10}H_2ClFeN_3O_5$
	480–680	570	44.724 (45.332)	$C_{10}H_2ClN_3O_4$	12.182 (12.724)	$0.5Fe_2O_3$
MnBCNR	165–220	175	6.301 (6.932)	$2H_2O$	93.536 (93.116)	$C_{24}H_{22}FMnN_5O_5$
	220–335	270	19.986 (20.342)	$C_6H_{14}N_2$	73.549 (73.874)	$C_{18}H_8FMnN_3O_5$
	335–480	365	21.202 (21.884)	C_8H_6F	52.348 (52.683)	$C_{10}H_2MnN_3O_5$
	480–675	540	39.931 (40.634)	$C_{10}H_2N_3O_4$	12.416 (23.216)	MnO
VOBCNR	205–340	260	20.928 (21.392)	$C_6H_{14}N_2$	79.212 (79.773)	$C_{18}H_8FN_3O_6V$
	340–470	370	22.200 (22.654)	C_8H_6F	57.012 (57.672)	$C_{10}H_2N_3O_6V$
	470–705	575	41.812 (42.318)	$C_{10}H_2N_3O_4$	15.201 (15.448)	VO_2

20.928% mass loss (calculated 21.392%) assigned to the release of $C_6H_{14}N_2$. The second step occurred between 340 and 470 °C (DTG 370 °C), showing a 22.200% loss (calculated 22.654%) corresponding to C_8H_6F, while the third step extended from 470 to 705 °C (DTG 575 °C), with a mass loss of 41.812% (calculated 42.318%) attributed to the decomposition

of $C_{10}H_2N_3O_4$. The final residue of 15.201% (calculated 15.448%) corresponds to VO_2.

Overall, the thermal data confirm that none of the complexes contain water of hydration, and the observed initial weight losses are solely due to coordinated water molecules. Accordingly, the FeBCNR, MnBCNR, and VOBCNR complexes contain one, two, and zero coordinated water molecules, respectively, consistent with the proposed molecular formulas [Fe(BC-H)(NR-H)Cl(H_2O)], [Mn(BC-H)(NR-H)(H_2O)$_2$], and [VO (BC-H)(NR-H)], supporting octahedral geometries for FeBCNR and MnBCNR and a square-pyramidal geometry for VOBCNR.

Conductivity measurements in ethanol further affirm the neutral, non-ionic nature of these complexes.[43] The molar conductivities are relatively low, with values of 9.85 μS cm^2 mol^{-1} for FeBCNR, 9.03 μS cm^2 mol^{-1} for MnBCNR, and 9.42 μS cm^2 mol^{-1} for VOBCNR (refer to Table S4). These values fall within the expected range for non-electrolytes, indicating that the chloride ion in FeBCNR is coordinated rather than existing as a dissociated counter-ion.

Electronic (UV-Vis) spectroscopy was used to investigate the electronic structure, geometry, and oxidation states of the synthesized complexes (Fig. S1). Solutions of the complexes were prepared at 1×10^{-3} mol L^{-1} concentration. The free ligands, 1*H*-benzimidazole-2-carboxylic acid (BC) and norfloxacin (NR), show intense n → π* and π → π* transitions in the range of 260–285 nm, corresponding to ligand-centered excitation. The metal complexes display additional low-intensity bands at lower energies: [Fe(BC-H)(NR-H)(Cl)(H_2O)] exhibits a band at 445 nm (≈22 472 cm^{-1}), [Mn(BC-H)(NR-H)(H_2O)$_2$] at 405 nm (≈24 691 cm^{-1}), and [VO(BC-H)(NR-H)] at 475 nm (≈21 053 cm^{-1}). These bands are relative to metal-to-ligand charge transfer (MLCT) or ligand-to-metal charge transfer (LMCT) contributions.[47–49] Specifically, the Fe(III) complex band can be assigned to a $^6A_{1g}(F) \rightarrow {}^4E_g(G)$ transition, consistent with an octahedral, low-spin d^5 configuration.[44] The Mn(II) complex band is consistent with a $^4T_{2g}(G) \rightarrow {}^6A_{1g}$ transition, typical for high-spin octahedral Mn(II) centers.[45] For the V(IV)O complex, the band is assigned to a $^2B_{2g} \rightarrow {}^2A_{1g}$ transition, characteristic of a square-pyramidal V(IV)O (V═O) core.[46]

Stoichiometric studies, employing Job's method of continuous variation,[47,48] reveal a metal : BC : NR ratio of 1 : 1 : 1 for all three complexes (see Fig. S2). This finding, when combined with IR and magnetic data, helps constrain the coordination number. Each ligand donates two atoms (one nitrogen and one oxygen), and two bidentate ligands provide four donor atoms to the metal center. To achieve a coordination number of six for FeBCNR and MnBCNR, two additional monodentate sites are required. In the case of VOBCNR, the V═O axial unit contributes one site, resulting in a total of five coordinated sites.

Mass spectrometric analyses were carried out using electron-ionization (EI) GC-MS and are therefore discussed as supportive molecular-weight evidence rather than high-resolution mass confirmation. The observed molecular ion peaks correspond to the expected molecular weight ranges of the proposed complexes and are consistent with their assigned formulations. The EI-MS spectra of FeBCNR, MnBCNR, and VOBCNR display molecular ion peaks or quasi-molecular fragments at *m*/*z* values consistent with the proposed formulations, within the expected deviation for EI-MS measurements. The observed peaks are assigned to the intact complexes or their stable fragments following the loss of coordinated water and/or labile ligands, which is typical for coordination compounds analyzed under electron ionization conditions. The observed molecular ions are: FeBCNR *m*/*z* = 589.4 (calculated formula $C_{24}H_{24}ClFeN_5O_6$, 588.8), MnBCNR *m*/*z* = 571.3 ($C_{24}H_{26}MnN_5O_7$, 570.4), and VOBCNR *m*/*z* = 545.6 ($C_{24}H_{22}VN_5O_6$, 546.4) (see Fig. S3). These peaks correspond to the neutral molecular formulas and support the presence of coordinated chloride and water molecules as proposed.

Integrating all the analytical techniques provides a coherent structural understanding of the complexes. Each BC and NR ligand functions as a bidentate, mono-anionic NO donor. For FeBCNR, the most accurate representation of the formula is [Fe(BC-H)(NR-H)(Cl)(H_2O)], where two bidentate NO ligands contribute four donor atoms, along with one coordinated chloride ion and one water molecule, resulting in an octahedral coordination sphere. In the case of MnBCNR, the data support the formula [Mn(BC-H)(NR-H)(H_2O)$_2$]; here, the two bidentate ligands, along with two water molecules, create a six-coordinate octahedral Mn(II) complex. For VOBCNR, the optimal description is [VO(BC-H)(NR-H)], where the chelating NO ligands occupy the equatorial positions, while the strong V═O bond occupies the axial position, leading to an overall square-pyramidal geometry.

The pH stability curves of the FeBCNR, MnBCNR, and VOBCNR complexes show a bell-shaped trend, indicating maximum stability around neutral pH (≈6–7). At low pH, protonation of donor sites weakens complex formation, while at high pH, hydrolysis or precipitation of metal hydroxides causes instability, as shown in Fig. S4.

3.2. DFT calculations

The electronic behavior of the free ligands and their corresponding metal complexes was explored using Density Functional Theory (DFT) calculations with the B3LYP functional. The optimized molecular geometries obtained from these computations are displayed in Fig. S5. Based on the optimized structures, the energies of the frontier molecular orbitals, HOMO and LUMO, were determined, allowing the calculation of the HOMO–LUMO energy gap (ΔE). These orbital energies were subsequently utilized to estimate various global reactivity parameters, such as chemical potential (μ), hardness (η), softness (σ), and the electrophilicity index (ω). A comprehensive overview of these computed parameters is summarized in Table S5.

Frontier molecular orbitals play a vital role in defining the electronic nature and reactivity of molecules. The spatial distribution of the HOMO and LUMO levels illustrates whether a compound is more inclined to donate or accept electrons during chemical interactions. For the studied systems, the computed HOMO and LUMO energies are listed in Table S5. Their corresponding orbital shapes are visualized in Fig. 2,

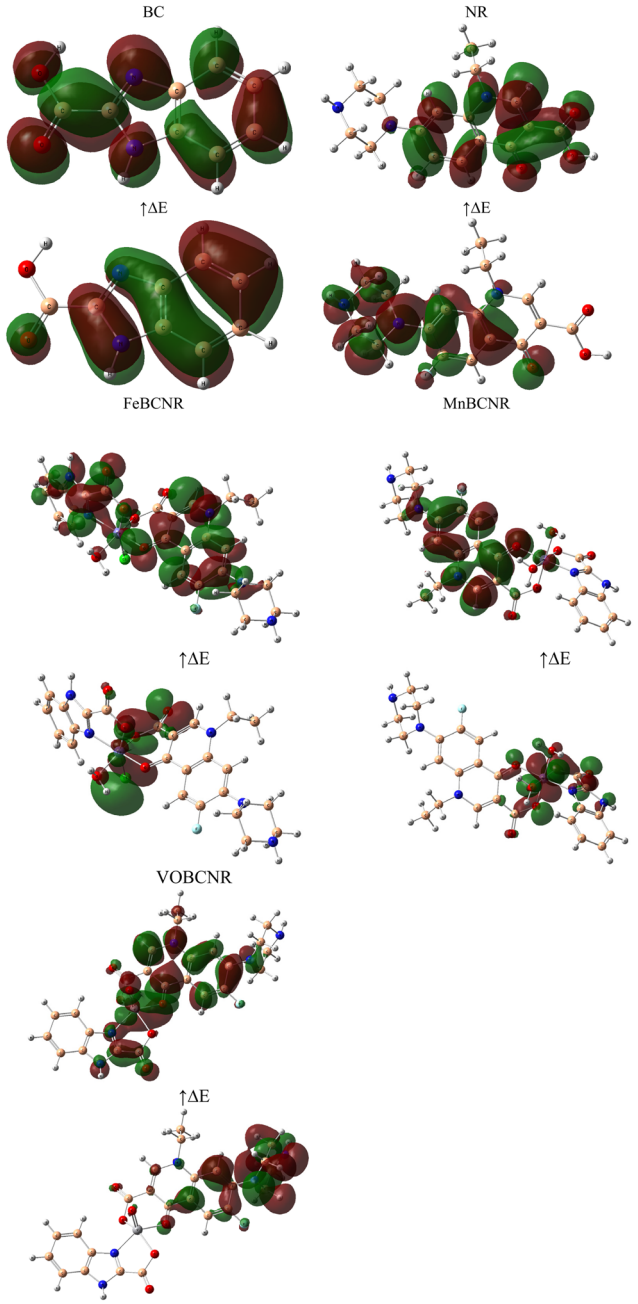

Fig. 2 Graphical three-dimensional representation of the frontier molecular orbitals (HOMO and LUMO) of BC, NR, FeBCNR, MnBCNR, and VOBCNR calculated at the optimized geometries. The orbitals are plotted using an isovalue of 0.02 a.u., where the green and red lobes represent positive and negative phases of the orbital wavefunction, respectively, illustrating the spatial distribution of electron density involved in frontier orbital interactions.

where the green and red contours represent the positive and negative phases of the orbitals, respectively, clearly identifying the regions most active in electron transfer and interaction processes.

The HOMO values reflect the electron-donating capability of the studied molecules. The BC ligand exhibits the lowest HOMO energy (−7.03 eV), indicating limited electron donation and thus lower expected biological reactivity. NR shows a higher HOMO (−5.86 eV), suggesting enhanced nucleophilic behavior and increased potential for interaction with biomolecular targets. Upon complexation, FeBCNR (−4.87 eV), MnBCNR (−6.14 eV), and VOBCNR (−5.26 eV) all display elevated HOMO energies relative to the free ligands, confirming that metal coordination enhances electron density at the frontier orbital. The relatively high HOMO values for FeBCNR and VOBCNR correlate with their strong antibacterial activity, consistent with their lower MIC values compared to the ligands. LUMO values represent the electron-accepting ability of the compounds. BC shows a relatively high LUMO (−2.09 eV), while NR has a slightly higher value (−1.73 eV), indicating weaker electron affinity compared to their metal complexes. FeBCNR (−2.11 eV), MnBCNR (−2.74 eV), and VOBCNR (−2.27 eV) show more stabilized LUMOs, which enhances their capacity to accept electrons during interaction with bacterial enzymes and DNA. Energy gap (ΔE) determines overall chemical reactivity. BC has the widest gap (4.94 eV), signifying high stability but low reactivity, consistent with its weak antibacterial response. NR has a narrower gap (4.13 eV), indicating better reactivity. Metal complexes significantly reduce ΔE values, with FeBCNR (2.76 eV), MnBCNR (3.39 eV), and VOBCNR (2.99 eV), reflecting enhanced biological reactivity through easier charge transfer. The lowest ΔE in FeBCNR aligns with its highest antibacterial potency, followed by VOBCNR and MnBCNR.

BC exhibits the highest Ionization Potential (IP) (7.03 eV), indicating difficulty in electron removal and thus reduced interaction capacity. NR shows a lower IP (5.86 eV), suggesting increased reactivity. The complexes demonstrate a further reduction: FeBCNR (4.87 eV), MnBCNR (6.14 eV), and VOBCNR (5.26 eV). The lowest IP of FeBCNR supports its superior ability to engage in electron transfer with biomolecular targets, explaining its strong antibacterial activity. Electron Affinity (EA) values reflect the tendency to accept electrons. BC (2.09 eV) and NR (1.73 eV) show modest affinity, while the complexes demonstrate stronger electron acceptance: FeBCNR (2.11 eV), MnBCNR (2.74 eV), and VOBCNR (2.27 eV). MnBCNR shows the highest EA, supporting its improved biological performance through enhanced binding interactions.

Electronegativity (χ) represents the overall electron-attracting capacity. BC has the highest value (4.56 eV), while NR is slightly lower (3.80 eV). The complexes show lower electronegativity values, with FeBCNR (3.49 eV), MnBCNR (4.44 eV), and VOBCNR (3.77 eV), reflecting improved electron delocalization upon metal coordination. This reduction in χ facilitates better orbital overlap with bacterial targets, enhancing activity. Chemical potential (μ) reflects system stability. BC (−4.56 eV) and NR (−3.80 eV) show strong negative potentials, indicative of less biological interaction. Metal complexation stabilizes μ values: FeBCNR (−3.49 eV), MnBCNR (−4.44 eV), and VOBCNR (−3.77 eV), allowing for more efficient charge transfer. FeBCNR and VOBCNR, with the least negative values, are the most reactive and biologically active.

Chemical hardness (η) values reflect resistance to electron cloud deformation. BC (2.47 eV) shows the highest hardness,[49] suggesting low reactivity and poor antibacterial activity. NR has lower hardness (2.07 eV), supporting better reactivity. Complexes show significantly reduced hardness: FeBCNR (1.38 eV), MnBCNR (1.70 eV), and VOBCNR (1.49 eV), reflecting improved biological efficiency. The lowest hardness of FeBCNR correlates with its superior antibacterial potency. Softness (σ), the reciprocal of hardness, indicates polarizability and biological reactivity. BC (0.20 eV) shows the lowest softness, consistent with weak activity. NR (0.24 eV) demonstrates moderate softness. Complexes are significantly softer: FeBCNR (0.36 eV), MnBCNR (0.29 eV), and VOBCNR (0.33 eV). The higher softness values enhance biomolecular interactions, explaining the superior antibacterial potency of the complexes.

The electrophilicity index (ω) reflects the tendency to accept electrons and stabilize interactions.[50] BC (4.21 eV) and NR (3.48 eV) show modest values. Metal complexes demonstrate enhanced electrophilicity, with FeBCNR (4.41 eV), MnBCNR (5.81 eV), and VOBCNR (4.75 eV). The high value of MnBCNR suggests a strong electrophilic character, aiding in interactions with bacterial nucleophiles. However, FeBCNR balances electrophilicity and softness better, explaining its slightly superior antibacterial performance. BC (0.24) and NR (0.29) show low Nucleophilicity Index (Nu) values, correlating with weak biological activity. Metal complexes show reduced values: FeBCNR (0.23), MnBCNR (0.17), and VOBCNR (0.21), indicating that their reactivity is more electrophilic than nucleophilic. This property favors strong interactions with bacterial electron-rich centers, enhancing antibacterial activity.

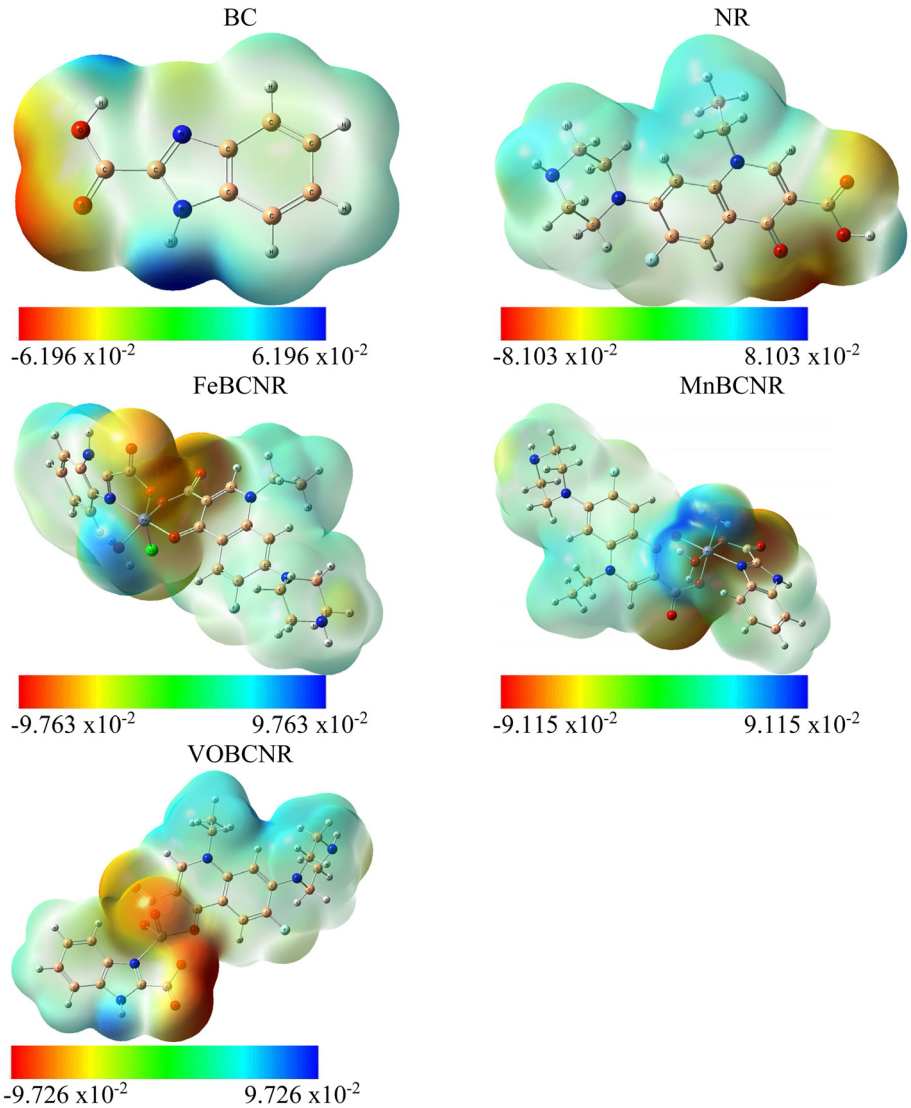

Fig. 3 Molecular electrostatic potential (MEP) maps of BC, NR, FeBCNR, MnBCNR, and VOBCNR mapped onto the electron density surface at 0.001 a.u. The color scale ranges from red (regions of negative electrostatic potential, electron-rich sites) through green (neutral) to blue (regions of positive electrostatic potential, electron-deficient sites), indicating the preferred regions for electrophilic and nucleophilic attack.

Computational descriptors clearly show that the complexation of BC and NR with Fe(III), Mn(II), and V(IV)O significantly enhances their electronic reactivity compared to the free ligands. Reduced energy gaps, lowered hardness, increased softness, and enhanced electrophilicity correlate strongly with improved antibacterial activity. Among the complexes, FeBCNR demonstrates the most favorable balance of parameters, followed closely by VOBCNR, while MnBCNR, though slightly less electronically reactive, maintains strong biological efficiency due to its high electrophilicity. The free ligands BC and NR show the weakest electronic properties, consistent with their low antibacterial activity. The overall order of predicted biological potency is: FeBCNR > VOBCNR > MnBCNR > NR > BC.

The Molecular Electrostatic Potential (MEP) map serves as an effective tool for illustrating how electron density is distributed across a molecule's surface.[51] It identifies regions susceptible to nucleophilic or electrophilic attack, thereby offering key insights into the potential interactions of ligands with protein active sites during docking analysis. In these maps, color gradations represent charge distribution: blue regions correspond to electron-deficient areas that tend to function as electrophilic centers, while red regions indicate electron-rich zones with notable nucleophilic character. The blue areas, generally appearing around hydrogen atoms, favor interactions with electron-donating residues within proteins. In contrast, the red zones typically envelop electronegative atoms such as oxygen and nitrogen, marking likely binding positions for electrophilic or positively charged species. As shown in Fig. 3, the MEP maps of the examined compounds reveal intense red regions around heteroatoms, implying a strong nucleophilic nature, whereas the blue areas near hydrogen atoms suggest a high potential for hydrogen bonding and dipolar interactions.

3.3. Biological activity

3.3.1. Antibacterial activity. The antibacterial screening revealed a pronounced difference between the activity of the free ligands and their corresponding metal complexes, as shown in Fig. 4, Tables S6 and S7. The ligands BC and NR exhibited only modest growth inhibition, with inhibition zones ranging from 8 to 11 mm, reflecting their limited ability to diffuse across bacterial membranes and interact with essential biomolecules. In contrast, the coordination of these ligands with transition metals led to a remarkable enhancement in activity. The FeBCNR, MnBCNR and VOBCNR complexes produced inhibition zones in the range of 21–28 mm, which are very close to those of the reference drug amoxicillin (25–30 mm). Notably, FeBCNR and VOBCNR were the most effective, exhibiting inhibition zones of 28 mm against *B. subtilis* and *S. aureus*, while also showing strong activity against Gram-negative strains (*E. coli*: 22–23 mm; *K. pneumoniae*: 24–25 mm). The results establish the order of antibacterial activity as FeBCNR ≈ VOBCNR > MnBCNR ≫ NR > BC, highlighting the impact of metal coordination in amplifying antibacterial potency, particularly against both Gram-positive and Gram-negative strains.

The activity index data corroborated the inhibition zone findings. The free ligands demonstrated weak antibacterial potential, with indices between 30 and 44% across all tested strains, indicating only one-third of the efficacy of amoxicillin. Upon complexation, dramatic improvements were observed. The FeBCNR and VOBCNR complexes reached activity indices of 92–93% against both Gram-positive and Gram-negative bacteria, essentially approaching the 100% activity of amoxicillin. MnBCNR also displayed high indices (84–93%), though slightly lower than those of FeBCNR and VOBCNR. These results clearly highlight that FeBCNR exhibited the most balanced and broad-spectrum activity, followed closely by VOBCNR, while MnBCNR was somewhat less effective but still far superior to the free ligands. The order of antibacterial efficacy, therefore, was FeBCNR ≥ VOBCNR > MnBCNR ≫ NR > BC.

3.3.2. Anti-fungal activity. The antifungal results revealed an enhancement upon complexation, as shown in Fig. 5, Tables S8 and S9. The free ligands BC and NR showed very weak inhibition against both *C. albicans* and *A. niger*, with inhibition zones of only 9–10 mm. This low activity underscores their limited antifungal potential. However, metal

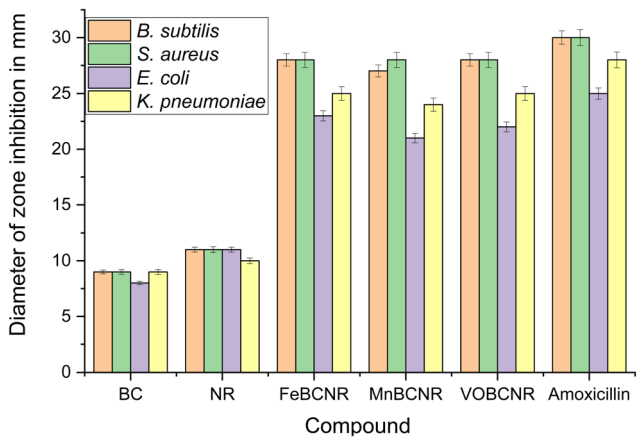

Fig. 4 Antibacterial activity as a diameter of zone inhibition in mm.

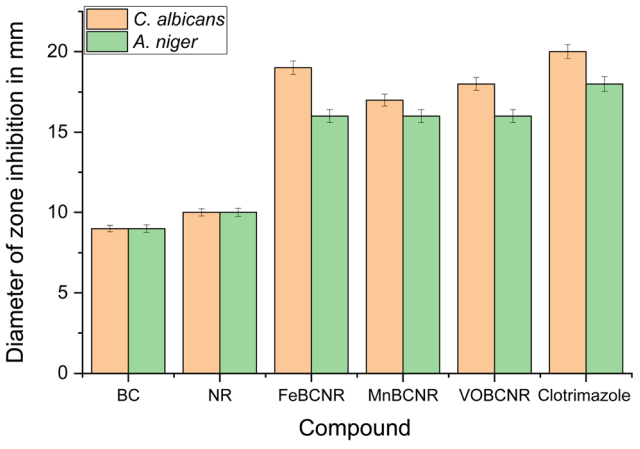

Fig. 5 Anti-fungal activity as a diameter of zone inhibition in mm.

coordination significantly amplified their antifungal action. FeBCNR exhibited the largest inhibition zones (19 mm against *C. albicans* and 16 mm against *A. niger*), almost equivalent to the activity of the standard drug clotrimazole (20 mm and 18 mm, respectively). VOBCNR and MnBCNR also produced inhibition zones of 16–18 mm, clearly superior to the free ligands. These findings emphasize the effectiveness of the complexes against both yeast and mold species, with FeBCNR being the most potent antifungal agent among the synthesized series.

The antifungal activity indices reflected the same trend as the inhibition zone measurements. The free ligands displayed negligible efficacy, with indices of 9–10%. In contrast, FeBCNR, VOBCNR, and MnBCNR demonstrated markedly improved indices of 16–19%, with FeBCNR again standing out as the most active (19% against *C. albicans*). Although none of the complexes reached the activity of clotrimazole (100%), their significantly higher values compared to the ligands indicate that metal coordination provides a substantial boost to antifungal potential. The antifungal activity order followed FeBCNR > VOBCNR ≈ MnBCNR ≫ NR > BC.

3.3.3. Antibacterial and antifungal activity (MIC, μM). The MIC values further validated the superiority of the metal complexes, as shown in Fig. 6 and Table S10. The free ligands exhibited poor activity, with MIC values of 100–120 μM across all bacterial and fungal strains, reflecting their weak efficacy. In contrast, FeBCNR and VOBCNR showed the lowest MIC values, particularly 70 μM against *E. coli* and *K. pneumoniae*, demonstrating excellent potency against Gram-negative bacteria. Both also maintained MIC values of 80 μM against fungi, which were markedly lower than those of the free ligands. MnBCNR displayed intermediate activity with MIC values of 80–90 μM, confirming its lower efficiency relative to FeBCNR and VOBCNR. The MIC results, therefore, consistently established the order of potency as FeBCNR ≈ VOBCNR > MnBCNR ≫ NR > BC, underscoring the improvement imparted by chelation.

3.3.4. Anti-inflammatory activity (mean percentage inhibition, %, and IC_{50}). The anti-inflammatory activity of the synthesized compounds was assessed using the egg albumin denaturation assay, where inhibition of heat-induced protein denaturation was monitored spectrophotometrically at 660 nm. The assay was performed at different concentrations (10–500 μM), with ibuprofen used as a reference drug, and results were expressed as percentage inhibition and IC_{50} values.

The anti-inflammatory assays demonstrated a strong concentration-dependent activity, as shown in Fig. 7 and Table S11.

The results reveal a clear concentration-dependent inhibition of protein denaturation for all tested compounds. The free ligands (BC and NR) exhibited weak anti-inflammatory responses, indicating limited intrinsic protein-stabilizing ability. In contrast, metal coordination markedly enhanced activity, particularly for MnBCNR and VOBCNR, which showed near-complete inhibition at higher concentrations.

This enhancement can be attributed to increased molecular rigidity, altered electronic distribution, and improved interaction with protein functional groups upon metal complexation. At low concentrations (10–50 μM), the free ligands BC and NR showed only minimal inhibition (3–14%), while the

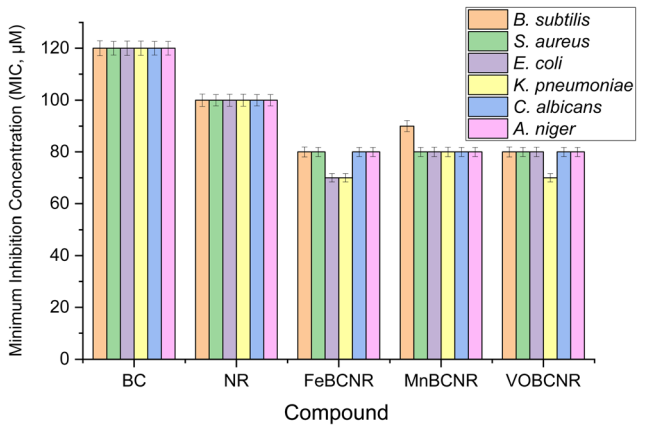

Fig. 6 Antibacterial and antifungal activity as the minimum inhibition concentration (MIC, μM).

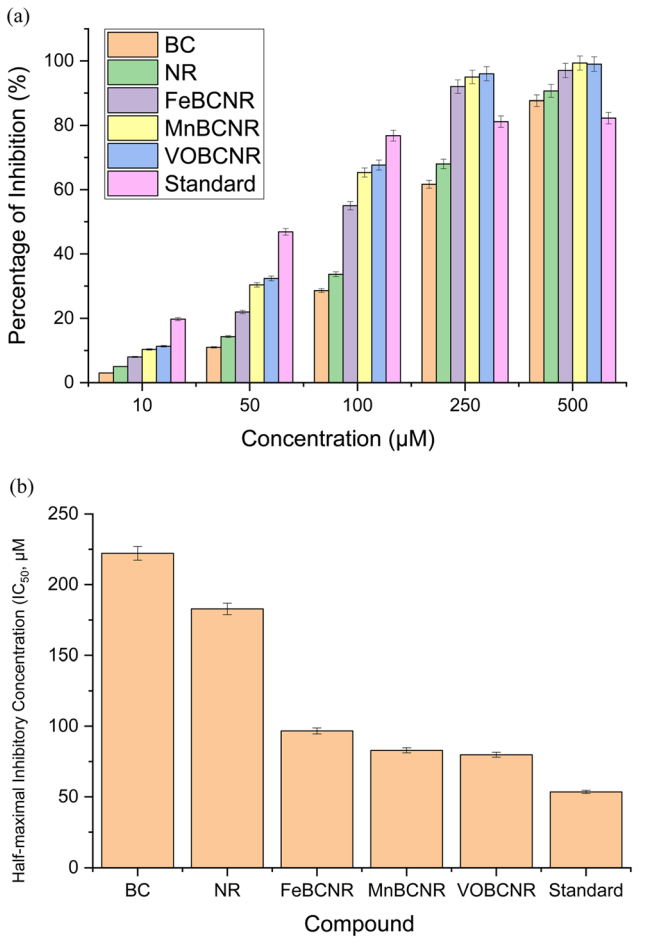

Fig. 7 Anti-inflammatory results as (a): mean percentage inhibition (%) and (b): IC_{50}.

metal complexes exhibited higher responses, particularly MnBCNR (30–65%) and VOBCNR (11–32%). At 100 μM, FeBCNR reached 55% inhibition, while MnBCNR and VOBCNR achieved 95% and 67%, respectively, approaching the standard drug (76.0%). At higher concentrations (250–500 μM), the metal complexes exhibited near-complete inhibition, with VOBCNR and MnBCNR exceeding 96–99%, surpassing the standard drug (81–82%).

The Half-maximal Inhibitory Concentration (IC_{50}) values confirmed this trend: VOBCNR (79.76 μM) exhibited the lowest IC_{50}, followed by MnBCNR (82.91 μM) and FeBCNR (96.64 μM), while BC and NR had much higher IC_{50} values (222.17 and 182.81 μM, respectively). The results, therefore, establish the order of anti-inflammatory efficacy as VOBCNR > MnBCNR > FeBCNR ≫ NR > BC.

The superior performance of VOBCNR, as evidenced by its lower IC_{50} values compared to other MnBCNR, FeBCNR, and free ligands as well as ibuprofen, suggests a stronger ability to stabilize protein structure against thermal denaturation. These findings highlight the crucial role of the metal center in modulating anti-inflammatory efficacy.

3.3.5. Correlation based on the chelation theory. The marked improvement in antibacterial, antifungal, and anti-inflammatory activities of the metal complexes compared to the free ligands can be rationalized by the chelation theory. Upon coordination, the metal ion engages in partial sharing of its positive charge with donor atoms in the ligand, which stabilizes the ligand framework and promotes electronic redistribution. These effects can enhance the reactivity of the complexes and strengthen their interactions with biomolecular targets. The consistent order of activity observed across all assays, FeBCNR ≈ VOBCNR > MnBCNR ≫ NR > BC, supports the principle that chelation amplifies biological efficacy and can modulate the reactivity of the complexes toward microbial and inflammatory targets.

3.3.6. Correlation with DFT parameters. The biological activities of the ligands and their complexes correlate strongly with the DFT-derived electronic descriptors. The free ligands BC and NR exhibited large energy gaps (ΔE = 4.94 and 4.13 eV), higher hardness (η = 2.47 and 2.07 eV), and lower softness values (σ = 0.20–0.24), consistent with their low reactivity and weak bioactivity. Upon complexation, the ΔE values decreased significantly (FeBCNR = 2.76, VOBCNR = 2.99, MnBCNR = 3.39 eV), which improved electron delocalization and enhanced reactivity. The increased softness (σ = 0.29–0.36) and electrophilicity indices (ω = 4.41–5.81) of the complexes explain their improved interaction with biological targets. FeBCNR, with the lowest ΔE and highest softness, correlated with its superior antibacterial and antifungal activity, while VOBCNR, with moderate ΔE but high electrophilicity, corresponded to its strongest anti-inflammatory effect. MnBCNR, despite slightly higher hardness, exhibited strong activity due to its high electronegativity (χ = 4.44) and electrophilicity (ω = 5.81). These results clearly demonstrate that the reduction in energy gap and the increase in electrophilicity and softness upon chelation are the key electronic factors driving enhanced biological activity.

3.4. Molecular docking

Molecular docking simulations have significantly advanced the fields of drug discovery and molecular biology by providing a fast and economical method to predict how molecules interact, their binding affinities, and potential biological functions.[52–54]

To ensure the reliability of the docking approach, a validation step was carried out through re-docking and superimposition using the native ligand, 1-ethyl-3-[8-methyl-5-(2-methylpyridin-4-yl)isoquinolin-3-yl]urea, which was originally co-crystallized with DNA gyrase B (PDB ID: 5MMN). The reproduced binding pose closely matched that of the experimental structure, confirming the accuracy and consistency of the docking procedure (Fig. S6).

Subsequently, the optimized docking studies were performed for the investigated compounds against the crystal structure of DNA gyrase B (PDB ID: 5MMN).[55–58] The simulations provided insights into the most favorable binding orientations of the free NR and CB ligands, along with their metal complexes FeCBNR, MnCBNR, and VOCBNR, as illustrated in Fig. 8, with detailed results summarized in Table S12.

The BC ligand exhibited weak interaction with DNA gyrase B, with a binding energy of −6.10 kcal mol^{-1}. The dominant stabilization arose from a hydrogen bond with ASP73 at 2.24 Å, supported by electrostatic interaction with ARG76 and hydrophobic contacts with ALA47 and VAL167 at longer distances (>4.8 Å). These interactions are relatively limited in number and strength, reflecting the poor antibacterial activity observed experimentally, where BC showed only small inhibition zones (8–9 mm) and high MIC values (120 μM). The restricted binding efficiency of BC highlights its weak ability to anchor within the active site of DNA gyrase B compared to the other compounds. NR demonstrated improved binding to DNA gyrase B with a docking score of −6.90 kcal mol^{-1}. The binding mode was stabilized by multiple hydrogen bonds with GLU50 (2.60–2.70 Å), a hydrogen bond with VAL43 (3.46 Å), and hydrophobic contacts with ILE78 and ILE94. A halogen bond with GLU50 further reinforced the ligand–protein interaction. These multiple, short-range interactions explain the better antibacterial activity of NR compared to BC, with inhibition zones of 10–11 mm and MIC values of 100 μM. However, despite this improvement, NR still displayed weaker binding than the metal complexes, consistent with its lower biological potency.

FeBCNR displayed strong and diverse interactions with DNA gyrase B, achieving a binding energy of −8.60 kcal mol^{-1}. The binding pocket stabilization involved three key hydrogen bonds with ASP73 (2.36 Å), VAL43 (2.65 Å), and GLU50 (2.77 Å). Additional contributions included an electrostatic interaction with ASP73, a halogen bond with ASN46, and hydrophobic contacts with ILE78 and ILE94. This combination of hydrogen bonding and multipolar interactions provides strong anchoring of the complex within the enzyme, explaining its good antibacterial potency, with inhibition zones of 23–28 mm and low MIC values (70–80 μM). The interactions of FeBCNR closely

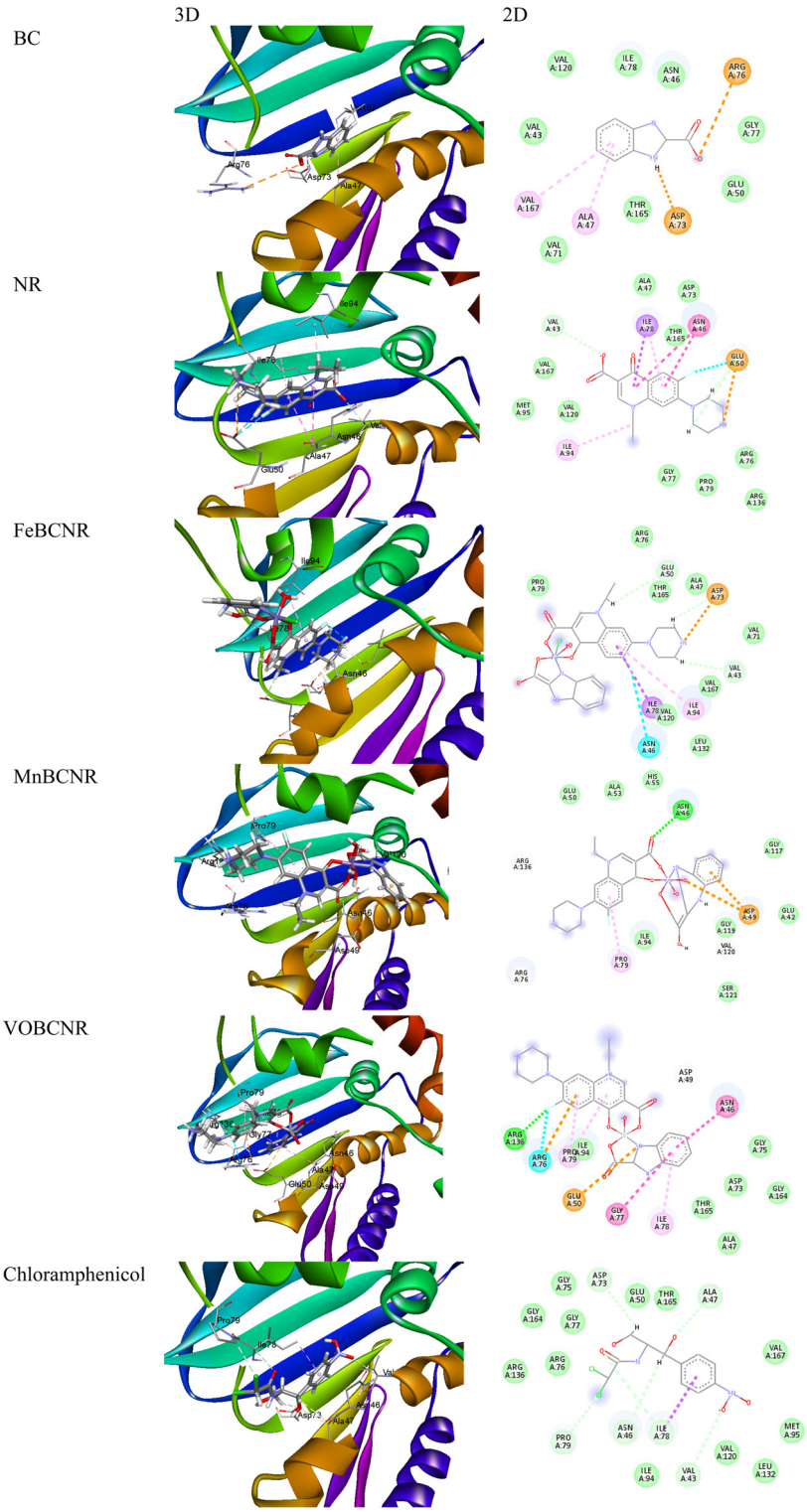

Fig. 8 3D and 2D representation of the BC and NR ligands and FeBCNR, MnBCNR, and VOBCNR complexes against *E. coli* DNA gyrase B (PDB ID: 5MMN) and its critical role in bacterial DNA replication and drug targeting.

resemble those of chloramphenicol, supporting its high efficacy. MnBCNR achieved a binding energy of −7.90 kcal mol^{-1}, slightly lower than FeBCNR and VOBCNR. The main stabilizing forces were a strong hydrogen bond with ASN46 (2.32 Å), electrostatic interactions with ASP49, and a hydrophobic contact with PRO79. Compared to FeBCNR, the MnBCNR complex formed fewer hydrogen bonds, which likely reduced its binding affinity. This difference is reflected in the

experimental antibacterial activity, where MnBCNR showed slightly smaller inhibition zones (21–28 mm) and higher MIC values (80–90 μM) relative to FeBCNR. Nevertheless, MnBCNR was markedly more active than the free ligands due to its enhanced docking interactions. VOBCNR exhibited a strong binding energy of −8.40 kcal mol^{-1}, comparable to FeBCNR. It formed a short hydrogen bond with ARG136 at 1.94 Å, supported by halogen and electrostatic interactions with ARG76 and GLU50, as well as multiple hydrophobic contacts with PRO79 and ILE78. This combination of polar and nonpolar interactions effectively stabilized the complex within the DNA gyrase B active site. Experimentally, VOBCNR demonstrated high antibacterial activity, with inhibition zones of 22–28 mm and MIC values (70–80 μM) close to FeBCNR, suggesting that docking predictions align with biological outcomes.

Comparison of the docking results reveals a clear trend in binding strength and interaction diversity: FeBCNR ≈ VOBCNR > MnBCNR > NR > BC. The free ligands exhibited weaker docking scores and fewer stabilizing interactions, correlating with their lower antibacterial potency. Metal complexation enhanced binding energies, reduced interaction distances, and introduced new types of interactions such as halogen bonds and stronger hydrogen bonding, thereby improving activity. FeBCNR and VOBCNR showed binding profiles closest to chloramphenicol, which explains their high antibacterial efficiency.

The molecular docking results correlate well with the *in vitro* antibacterial findings. Compounds with higher binding affinity and stronger interactions (FeBCNR and VOBCNR) displayed larger inhibition zones (23–28 mm) and lower MIC values (70–80 μM). MnBCNR, with slightly fewer stabilizing contacts, showed moderate activity (21–28 mm, MIC 80–90 μM). The free ligands BC and NR, which exhibited weak and limited binding, correspondingly showed poor activity, with small inhibition zones (8–11 mm) and high MIC values (100–120 μM). Thus, the docking studies provide strong mechanistic support for the observed antibacterial results, suggesting that enhanced ligand–enzyme interactions directly translate into improved biological activity.

4. Conclusion

The combined experimental, theoretical, and biological investigations demonstrate that the newly synthesized Fe(III) (FeBCNR), Mn(II) (MnBCNR), and V(IV)O (VOBCNR) complexes form stable, well-defined coordination systems, with BC and NR acting as bidentate NO donors. Structural characterization indicates that FeBCNR and MnBCNR adopt octahedral geometries, while VOBCNR exhibits a square-pyramidal configuration. Spectroscopic, magnetic, and thermal analyses support the proposed coordination environments. DFT calculations show a reduction in the HOMO–LUMO gap (2.76–3.39 eV) and changes in electronic descriptors, indicating increased electron delocalization and reactivity. Among the investigated compounds, the oxidovanadium(IV) complex (VOBCNR) emerges as the most promising anti-inflammatory agent, exhibiting the lowest IC_{50} value (IC_{50} = 79.76 μM) and the highest inhibition efficiency compared to the manganese(II) and iron(III) complexes. Molecular docking suggests potential interactions of the complexes with DNA gyrase B, providing insights into possible binding modes but not confirming experimental binding. Overall, this study shows that metal coordination enhances the stability, electronic properties, and biological activity of the ligands.

Author contributions

H. M. Abd El-Lateef: investigation, resources, formal analysis, funding acquisition, writing – original draft, and writing – review & editing. M. M. Khalaf: investigation, resources, formal analysis, funding acquisition, writing – original draft, and writing – review & editing. A. Abdou: investigation, methodology, resources, formal analysis, data curation, funding acquisition, writing – original draft, and writing – review & editing.

Conflicts of interest

The authors declare that they have no known competing financial interests or personal relationships that could have appeared to influence the work reported in this paper.

Data availability

The authors confirm that the data supporting the findings of this study are available within the article and its supplementary information (SI). Supplementary information is available. See DOI: https://doi.org/10.1039/d5dt02558c.

Acknowledgements

This work was supported by the Deanship of Scientific Research, Vice Presidency for Graduate Studies and Scientific Research, King Faisal University, Saudi Arabia [Grant No. KFU254642].

References

1 L. Morrison and T. R. Zembower, Antimicrobial resistance, *Gastrointest. Endosc. Clin.*, 2020, **30**(4), 619–635.
2 H. D. Marston, D. M. Dixon, J. M. Knisely, T. N. Palmore and A. S. Fauci, Antimicrobial resistance, *J. Am. Med. Assoc.*, 2016, **316**(11), 1193–1204.
3 J. Acar and B. Rostel, Antimicrobial resistance: an overview, *Rev. Sci. Tech*, 2001, **20**(3), 797–810.
4 S. C. Ng, H. Y. Shi, N. Hamidi, F. E. Underwood, W. Tang, E. I. Benchimol, R. Panaccione, S. Ghosh, J. C. Wu and F. K. Chan, Worldwide incidence and prevalence of inflammatory bowel disease in the 21st century: a systematic

review of population-based studies, *Lancet*, 2017, **390**(10114), 2769–2778.
5 K. Foo and D. Roofeh, *Inflammatory diseases, Pediatric Rotations: A Quick Guide for Medical Students*, Springer, 2024, pp. 335–348.
6 E. Banin, D. Hughes and O. P. Kuipers, Bacterial pathogens, antibiotics and antibiotic resistance, *FEMS Microbiol. Rev.*, 2017, **41**(3), 450–452.
7 N. Cassir, J.-M. Rolain and P. Brouqui, A new strategy to fight antimicrobial resistance: the revival of old antibiotics, *Front. Microbiol.*, 2014, **5**, 551.
8 J. M. Bennett, G. Reeves, G. E. Billman and J. P. Sturmberg, Inflammation–nature's way to efficiently respond to all types of challenges: implications for understanding and managing "the epidemic" of chronic diseases, *Front. Med.*, 2018, **5**, 316.
9 E. J. Goldstein, Norfloxacin, a fluoroquinolone antibacterial agent: classification, mechanism of action, and in vitro activity, *Am. J. Med.*, 1987, **82**(6), 3–17.
10 A. R. Millanao, A. Y. Mora, N. A. Villagra, S. A. Bucarey and A. A. Hidalgo, Biological effects of quinolones: a family of broad-spectrum antimicrobial agents, *Molecules*, 2021, **26**(23), 7153.
11 M. Arshad, M. S. Khan and S. A. Nami, Norfloxacin analogues: Drug likeness, synthesis, biological, and molecular docking assessment, *Russ. J. Bioorg. Chem.*, 2021, **47**(2), 483–495.
12 P. A. Thakurdesai, S. G. Wadodkar and C. T. Chopade, Synthesis and anti-inflammatory activity of some benzimidazole-2-carboxylic acids, *Pharmacologyonline*, 2007, **1**, 314–329.
13 E. B. Şaş, S. Çifçi and M. Kurt, Spectroscopic Characterization and DFT Calculations on 1H-benzimidazole-2-carboxylic acid monohydrate Molecule, *Sak. Univ. J. Sci.*, 2022, **26**(5), 879–891.
14 K. S. Suvaiv, S. M. Hasan, S. P. Kushwaha, A. Kumar, I. Z. Ahmad and P. Kumar, Design, Molecular Docking, Synthesis, and Antibacterial Activity of 1H-Benzimidazole-2-Carboxylic Acid (2-Oxo-1, 2-Dihydro-Indol-3-Ylidene)-Hydrazide Derivatives, *Indian J. Heterocycl. Chem.*, 2023, **33**(02), 249–256.
15 S. Rafique, M. Idrees, A. Nasim, H. Akbar and A. Athar, Transition metal complexes as potential therapeutic agents, *Biotechnol. Mol. Biol. Rev.*, 2010, **5**(2), 38–45.
16 A. Bagchi, P. Mukherjee and A. Raha, A review on transition metal complex-mordern weapon in medicine, *Int. J. Recent Adv. Pharm. Res.*, 2015, **5**, 171–180.
17 K. Thakur and A. R. Pathania, An overview of metal ions and their complexes in biological processes as therapeutic agent, in *AIP Conference Proceedings*, AIP Publishing LLC, 2025, p. 060001.
18 I. Kostova and S. Balkansky, Metal complexes of biologically active ligands as potential antioxidants, *Curr. Med. Chem.*, 2013, **20**(36), 4508–4539.
19 J. D. Aguirre and V. C. Culotta, Battles with iron: manganese in oxidative stress protection, *J. Biol. Chem.*, 2012, **287**(17), 13541–13548.
20 A. A. Sharfalddin, I. M. Al-Younis, H. A. Mohammed, M. Dhahri, F. Mouffouk, H. Abu Ali, M. J. Anwar, K. A. Qureshi, M. A. Hussien and M. Alghrably, Therapeutic properties of vanadium complexes, *Inorganics*, 2022, **10**(12), 244.
21 R. Singh and A. Chaudhary, Biologically relevant tetraaza-macrocyclic complexes of manganese: synthetic, spectral, antimicrobial, antifertility and antiinflammatory approach, *J. Inorg. Biochem.*, 2004, **98**(11), 1712–1721.
22 D. Kovala-Demertzi, D. Hadjipavlou-Litina, M. Staninska, A. Primikiri, C. Kotoglou and M. A. Demertzis, Anti-oxidant, in vitro, in vivo anti-inflammatory activity and antiproliferative activity of mefenamic acid and its metal complexes with manganese(II), cobalt(II), nickel(II), copper(II) and zinc(II), *J. Enzyme Inhib. Med. Chem.*, 2009, **24**(3), 742–752.
23 R. K. Mohapatra and M. Kudrat-E-Zahan, Antimicrobial activity of Mn complexes incorporating Schiff bases: A short review, *Sci. Rev. Chem. Commun.*, 2019, **5**, 27–36.
24 N. Muhammad, S. Ali, S. Shahzadi and A. Khan, Oxovanadium(IV) complexes of non-steroidal anti-inflammatory drugs: Synthesis, spectroscopy, and antimicrobial activity, *Russ. J. Coord. Chem.*, 2008, **34**(6), 448–453.
25 K. Hashmi, A. Satya, P. Mishra, E. Veg, T. Khan and S. Joshi, The Potentiality of Vanadium Complexes as Antibacterial Agents, *Eng. Proc.*, 2025, **87**(1), 91.
26 C. Datta, D. Das, P. Mondal, B. Chakraborty, M. Sengupta and C. R. Bhattacharjee, Novel water soluble neutral vanadium(IV)–antibiotic complex: Antioxidant, immunomodulatory and molecular docking studies, *Eur. J. Med. Chem.*, 2015, **97**, 214–224.
27 S. Shukla and A. Mishra, Metal complexes used as anti-inflammatory agents: Synthesis, characterization and anti-inflammatory action of VO (II)-complexes, *Arabian J. Chem.*, 2019, **12**(7), 1715–1721.
28 M. Barančoková, D. Kikelj and J. Ilaš, , Recent progress in the discovery and development of DNA gyrase B inhibitors, *Future Med. Chem.*, 2018, **10**(10), 1207–1227.
29 F. Neese, Software update: The ORCA program system—version 6.0, *Wiley Interdiscip. Rev.:Comput. Mol. Sci.*, 2025, **15**(2), e70019.
30 A. Schäfer, C. Huber and R. Ahlrichs, Fully optimized contracted Gaussian basis sets of triple zeta valence quality for atoms Li to Kr, *J. Chem. Phys.*, 1994, **100**(8), 5829–5835.
31 F. Weigend and R. Ahlrichs, Balanced basis sets of split valence, triple zeta valence and quadruple zeta valence quality for H to Rn: Design and assessment of accuracy, *Phys. Chem. Chem. Phys.*, 2005, **7**(18), 3297–3305.
32 P. Mamta and A. Chaudhary, Synthesis, spectroscopic elucidation, density functional theory calculation, and molecular docking studies of a novel series of tetradentate macrocyclic Schiff base ligands and their Zn(II) complexes and investigations of their antimicrobial, anti–inflammatory, and anticancer activities, *Appl. Organomet. Chem.*, 2024, **38**(2), e7330.
33 M. D. Hanwell, D. E. Curtis, D. C. Lonie, T. Vandermeersch, E. Zurek and G. R. Hutchison,

Avogadro: an advanced semantic chemical editor, visualization, and analysis platform, *J. Cheminf.*, 2012, **4**, 1–17.
34 T. Lu and F. Chen, Multiwfn: A multifunctional wavefunction analyzer, *J. Comput. Chem.*, 2012, **33**(5), 580–592.
35 M. Miar, A. Shiroudi, K. Pourshamsian, A. R. Oliaey and F. Hatamjafari, Theoretical investigations on the HOMO–LUMO gap and global reactivity descriptor studies, natural bond orbital, and nucleus-independent chemical shifts analyses of 3-phenylbenzo[d]thiazole-2(3H)-imine and its para-substituted derivatives, Solvent and substituent effects, *J. Chem. Res.*, 2020, **45**(1–2), 147–158.
36 V. Choudhary, A. Bhatt, D. Dash and N. Sharma, DFT calculations on molecular structures, HOMO–LUMO study, reactivity descriptors and spectral analyses of newly synthesized diorganotin(IV) 2-chloridophenylacetohydroxamate complexes, *J. Comput. Chem.*, 2019, **40**(27), 2354–2363.
37 A. E. Saidi, N. Bouzidi, M. Ziane, M. Gherib, C. Rahila and M. Mioc, In silico and in vitro studies: investigating the chemical composition, DFT, molecular docking, and dynamic simulation of Satureja candidissima (Munby) Briq essential oil as a potential antibacterial agent, *J. Biomol. Struct. Dyn.*, 2025, **43**(8), 4043–4062.
38 H. M. Abd El-Lateef, M. M. Khalaf, M. Kandeel and A. Abdou, Synthesis, Characterization, DFT, Biological and Molecular Docking of Mixed Ligand Complexes of Ni(II), Co(II), and Cu(II) Based on Ciprofloxacin and 2-(1H-benzimidazol-2-yl)phenol, *Inorg. Chem. Commun.*, 2023, **155**, 111087.
39 H. M. Abd El-Lateef, M. M. Khalaf, F. El-Taib Heakal and A. Abdou, Fe(III), Ni(II), and Cu(II)-moxifloxacin-tri-substituted imidazole mixed ligand complexes: Synthesis, structural, DFT, biological, and protein-binding analysis, *Inorg. Chem. Commun.*, 2023, **158**, 111486.
40 D. Rehder, *Bioinorganic vanadium chemistry*, John Wiley & Sons, 2008.
41 E. J. Baran, Spectroscopic studies of oxovanadium coordination compounds, *J. Coord. Chem.*, 2001, **54**(3–4), 215–238.
42 A. A. Nejo, *Metal (ii) schiff base complexes and the insulin-mimetic Studies on the oxovanadium(iv) complexes*, 2009.
43 I. Ali, W. A. Wani and K. Saleem, Empirical formulae to molecular structures of metal complexes by molar conductance, *Syn. React. Inorg. Metaorg. Nanometal. Chem.*, 2013, **43**(9), 1162–1170.
44 G. A. Al-Hazmi, K. S. Abou-Melha, N. M. El-Metwaly, I. Althagafi, F. Shaaban and R. Zaky, Green synthesis approach for Fe(III), Cu(II), Zn(II) and Ni(II)–Schiff base complexes, spectral, conformational, MOE–docking and biological studies, *Appl. Organomet. Chem.*, 2020, **34**(3), e5403.
45 S. M. Morgan, A. El-Sonbati and H. Eissa, Geometrical structures, thermal properties and spectroscopic studies of Schiff base complexes: Correlation between ionic radius of metal complexes and DNA binding, *J. Mol. Liq.*, 2017, **240**, 752–776.
46 N. El-Metwaly, I. Althagafi, H. A. Katouah, J. H. Al-Fahemi, T. M. Bawazeer and A. M. Khedr, Synthesis of novel VO (II)–thaizole complexes; spectral, conformational characterization, MOE–docking and genotoxicity, *Appl. Organomet. Chem.*, 2019, **33**(9), e5095.
47 A. Gahlan, M. El-Mottaleb, N. Badawy, F. Kamale and S. H. Ali, Spectrophotometeric studies on binary and ternary complexes of some metal ions with alizarin red S and cysteine, *Int. J. Adv. Res.*, 2014, **2**(10), 570–584.
48 R. M. El-Khatib and L. A.-M. E. Nassr, Spectrophotometric study of some Mn(II) ternary complexes and their analytical applications, *Monatsh. Chem.*, 2009, **140**, 1139–1142.
49 T. Murugan, R. Venkatesh, K. Geetha and A. Abdou, Synthesis, spectral investigation, DFT, antibacterial, antifungal and molecular docking studies of Ni(II), Zn(II), Cd (II) complexes of tetradentate Schiff-base ligand, *Asian J. Chem.*, 2023, **35**(6), 1509–1517.
50 D. Alhashmialameer, G. G. Mohamed, Y. Al-hawamy, A. Abdou, H. A. Alshehri, F. Alkhatib and A. M. Abu-Dief, Fabrication, preparation, physicochemical characterization, and theoretical studies of some novel Schiff base ciprofloxacin metal complexes: DNA interaction and biomedical applications, *Appl. Organomet. Chem.*, 2024, **38**(11), e7667.
51 M. M. Khalaf, H. M. Abd El-Lateef, M. Gouda, A. A. Abdelhamid, M. Abdelbaset, A. H. Alsulami, M. N. Almarri and A. Abdou, Designing, DFT, biological, & molecular docking analysis of new Iron(III) & copper(II) complexes incorporating 1-{[-(2-Hydroxyphenyl) methylene] amino}– 5, 5-diphenylimidazolidine-2, 4-dione (PHNS), *Comput. Biol. Chem.*, 2024, **109**, 108031.
52 E. Okpo, A. Agboke, C. Udobi, G. John and I. Andy, The synergy of molecular docking and bioinformatics: An in depth review in drug discovery, *Biotechnol. J. Int.*, 2024, **28**(4), 119–136.
53 T. Lanez, M. Feizi-Dehnayebi and E. Lanez, Assessment of the electrostatic binding of ferrocenylmethyl-nitroaniline derivatives to DNA: A combined experimental and theoretical study, *J. Mol. Struct.*, 2024, **1308**, 138386.
54 A. M. El-Saghier, S. S. Enaili, A. Abdou, A. Y. Alzahrani, S. Ben Moussa, M. A. Gad and A. M. Kadry, Thiadiazole/thiadiazine derivatives as insecticidal agent: design, synthesis, and biological assessment of 1, 3, 4-(thiadiazine/thiadiazole)-benzenesulfonamide derivatives as IGRs analogues against Spodoptera littoralis, *J. Agric. Food Chem.*, 2024, **72**(20), 11369–11380.
55 F. Jalali-Yazdi, S. Chowdhury, C. Yoshioka and E. Gouaux, Mechanisms for zinc and proton inhibition of the GluN1/GluN2A NMDA receptor, *Cell*, 2018, **175**(6), 1520–1532.
56 A. Marchese and E. A. Debbia, The role of gyrA, gyrB, and dnaA functions in bacterial conjugation, *Ann. Microbiol.*, 2016, **66**(1), 223–228.
57 S. N. Dighe and T. A. Collet, Recent advances in DNA gyrase-targeted antimicrobial agents, *Eur. J. Med. Chem.*, 2020, **199**, 112326.
58 A. Abdel-Aziem, H. Abdelmegeed, M. S. Abdel-Aziz, G. Kirsch and E. R. El-Sawy, New heterocycles from dehydroacetic acid (DHA). Synthesis, antimicrobial activity, DNA gyrase inhibition, antioxidant activity, and molecular docking study, *J. Mol. Struct.*, 2025, **1321**, 139786.